Reaction-Diffusion Modelling for the Cross-Linking of Actin Gels

Kishore Basu[*][1], Ondrej Maxian[†][1], and Aleksandar Donev[‡][1]

[1]Courant Institute of Mathematical Sciences, New York University

August 5, 2021

Abstract

We expand upon the Split Reactive Brownian Dynamics (SRBD) algorithm for reaction-diffusion modelling, whereby particles diffuse, and also react when within a chosen reactive radius. We extend this algorithm to allow for the numerical simulation of dimers. To do so, we employ several temporal integrators to simulate Langevin stochastic differential equations, and assess their convergence properties. We investigate the various competing time scales that are relevant to the simulation of dimers, and develop a new integration scheme for evolving Brownian motion on the unit sphere. We show that this integration scheme minimizes inaccuracies and numerical instability in our model, especially when solving stiff equations.

1 INTRODUCTION AND BACKGROUND

It is well understood that complex biological processes are governed by monomers assembled into larger units called polymers. The simplest example of this is a dimer. These dimers are crucial in the organization of macroscopic structures, such as the cell cytoskeleton. Biologists have frequently made experimental observations of the cross linking of actin polymers by dimers aptly named cross linkers. However, there is little mathematical theory devoted to their diffusion. These cross linkers evolve dynamically, binding and unbinding with actin filaments to provide structure, support, and elasticity to the cell. When not bound, they freely diffuse as a dimer. Consistent with the main goals of statistical mechanics, we set out to create a model of the cell cytoskeleton without assuming any macroscopic laws, but by looking at the aggregate behaviour of microscopic entities.

Our goal was to extend the stochastic hydrodynamic toolbox detailed in [1], in order to allow for the simulation of dimers. Previously this toolbox was designed to handle monomers, which diffuse independently. This toolbox uses Stochastic Reactive Brownian Dynamics (SRBD) for reaction-diffusion modelling, whereby particles diffuse freely by a continuous random walk. When they encounter another particle within a reactive distance a_r, they react with a specified Poisson rate.

---

[*]kb4063@courant.nyu.edu
[†]om759@nyu.edu
[‡]donev@courant.nyu.edu

For our purposes, a_r represents the actin binding domain. SRBD runs particle simulations by creating a box, known as a Doi box, partitioned into a grid. Each grid cell has a size larger than the maximal reactive radius, so that each reaction must occur within a single cell. We also study another method, Split Brownian Dynamics with Reaction Master Equation (S-BD-RME) where we process diffusion similarly, however, rather than reacting when within a_r, reactions are processed only when particles are in the same reactive cell.

Our simulation is made difficult by its reaction-limited nature. Each individual cross linker will diffuse until it encounters an actin polymer. The translational, rather than rotational, movement of the cross linker is relevant in this step. However, this movement will likely take an exceedingly long time. Thus, we want to develop an integrator with minimal error for translational diffusion when ran with a large time step size, Δt. When the dimer binds to actin, the relevant movement is no longer translational, but rotational. Once one end of a dimer has bound, the dimer will rotate in order to bind to another actin filament. Therefore, it is ideal if we can develop a way to evolve the rotational movement of the cross linker analytically. In addition, we would like to create a model that can be used for dimers with varying bond strengths (stiffness), as this will increase the biological plausibility of our model.

We start by describing the model we use to simulate dimers. Then we compare and evaluate various methods by which these differential equations could be integrated. We then quantify the rotational movement of the dimer by computing the rotational diffusion coefficient, and develop a method using an Euler-Lie integrator to evolve Brownian motion on the unit sphere semi-analytically. Finally, we detail certain instances when the theory of rotational diffusion may break down.

2 Mathematical Model

We begin by constructing a mathematical model for the displacement of a molecule r while in a thermodynamic driving potential, U. This can be done by looking at the overdamped Langevin equation,

$$m\frac{d^2\boldsymbol{r}}{dt^2} = -\frac{\partial U}{\partial \boldsymbol{r}} - \mu^{-1}\frac{d\boldsymbol{r}}{dt} + \sqrt{2k_bT\mu^{-1}}\frac{d\boldsymbol{W}}{dt}, \tag{1}$$

where m, k_b, T, μ, $d\boldsymbol{W}$, are the mass, Boltzmann's constant, temperature, mobility coefficient, and the differential of the Wiener process in $\mathbb{R}^d$ respectively. In the low-intertia limit, $m \to 0$, we are left with

$$d\boldsymbol{r} = -\mu\frac{\partial U}{\partial \boldsymbol{r}}dt + \sqrt{2k_bT\mu}\ d\boldsymbol{W}. \tag{2}$$

Note that by definition, $\partial U/\partial \boldsymbol{r} = -\boldsymbol{F}$. Each cross linker is composed of two molecules, $\boldsymbol{r}_1$, $\boldsymbol{r}_2 \in \mathbb{R}^d$, of radii a_1, and a_2, respectively, and are modelled to be connected by a spring of stiffness k. Thus, the Langevin equation we model is

$$d\boldsymbol{r}_i = \mu_i\boldsymbol{F}_idt + \sqrt{2D_i}\ d\boldsymbol{W}_i(t), \tag{3}$$

where μ_i, $D_i = k_b T \mu_i$, $\boldsymbol{F}_i$ are the mobility coefficient, diffusion coefficient, and spring force, for molecule i, respectively. By the Stokes-Einstein law, we know that for perfectly spherical objects in a fluid with low Reynolds number, $D = k_b T \mu = k_b T / (6 \pi \eta a)$, where, η is the dynamic viscosity, and a is the hydrodynamic radius of the molecule. The solution of (3) will follow an Ornstein-Uhlenbeck process, if $\boldsymbol{F}_i$ is linear in $\boldsymbol{r}_i$.

2.1 CENTER OF MASS AND RELATIVE DISTANCE

We can judiciously change coordinate systems from $(\boldsymbol{r}_1, \boldsymbol{r}_2)$ to $(\boldsymbol{r}_{\text{cm}}, \boldsymbol{r}_{\text{d}})$, where $\boldsymbol{r}_{\text{cm}}$ is the position of the center of mobility, and $\boldsymbol{r}_{\text{d}}$ is the position of $\boldsymbol{r}_1 - \boldsymbol{r}_2$. This is important because, as we will see, $\boldsymbol{r}_{\text{cm}}$ will be entirely characterized by Brownian motion, and therefore the translational movement of the dimer can be analytically solved. Suppose that we wish to track the movement of the center of mobility, $d\boldsymbol{r}_{\text{cm}}$, given by $d\boldsymbol{r}_{\text{cm}} = \alpha d\boldsymbol{r}_1 + (1 - \alpha) d\boldsymbol{r}_2$ for $\alpha \in (0, 1)$. Then,

$$
\begin{aligned}
d\boldsymbol{r}_{\text{cm}} &= \alpha d\boldsymbol{r}_1 + (1 - \alpha) d\boldsymbol{r}_2, \\
&= \alpha \left(\mu_1 \boldsymbol{F}_1 dt + \sqrt{2 k_b T \mu_1}\, d\boldsymbol{W}_1(t) \right) + (1 - \alpha) \left(\mu_2 \boldsymbol{F}_2 dt + \sqrt{2 k_b T \mu_2}\, d\boldsymbol{W}_2(t) \right), \\
&= \boldsymbol{F}_1 \left(\alpha \mu_1 - (1 - \alpha) \mu_2 \right) dt + \alpha \left(\sqrt{2 k_b T \mu_1}\, d\boldsymbol{W}_1(t) \right) + (1 - \alpha) \left(\sqrt{2 k_b T \mu_2}\, d\boldsymbol{W}_2(t) \right),
\end{aligned}
$$

where we have used the fact that $\boldsymbol{F}_1 = -\boldsymbol{F}_2$. Note that the center of mobility will occur when $\alpha = \mu_2 / (\mu_1 + \mu_2)$, and the deterministic terms will cancel, leaving us with

$$
\begin{aligned}
d\boldsymbol{r}_{\text{cm}} &= \frac{\mu_2}{\mu_1 + \mu_2} \left(\sqrt{2 k_b T \mu_1}\, d\boldsymbol{W}_1(t) \right) + \frac{\mu_1}{\mu_1 + \mu_2} \left(\sqrt{2 k_b T \mu_2}\, d\boldsymbol{W}_2(t) \right), \\
&= \left(\sqrt{\frac{2 k_b T \mu_2^2 \mu_1}{(\mu_1 + \mu_2)^2}}\, d\boldsymbol{W}_1(t) \right) + \left(\sqrt{\frac{2 k_b T \mu_1^2 \mu_2}{(\mu_1 + \mu_2)^2}}\, d\boldsymbol{W}_2(t) \right), \\
&= \sqrt{\frac{2 k_b T \mu_1 \mu_2}{(\mu_1 + \mu_2)}}\, d\boldsymbol{W}_3(t),
\end{aligned}
$$

since $d\boldsymbol{W}_1(t)$ and $d\boldsymbol{W}_2(t)$ are independent Wiener processes and their variances will add. Thus, in general, the diffusion coefficient of the center of mobility is given by $D_{\text{cm}} = k_b T \mu_1 \mu_2 / (\mu_1 + \mu_2)$. We can write this a simpler way by reintroducing an effective mobility coefficient, μ_{cm}, such that

$$
d\boldsymbol{r}_{\text{cm}} = \sqrt{2 k_b T \mu_{\text{cm}}}\, d\boldsymbol{W}_3(t), \tag{4}
$$

where $\mu_{\text{cm}}^{-1} = \mu_1^{-1} + \mu_2^{-1}$. However, the simplest case to consider is when both molecules have the same radius. Then $\mu = \mu_1 = \mu_2$, implying $\alpha = 0.5$, and $D_1 = D_2 = D$. In addition, we can see that in this case,

$$
\begin{aligned}
d\boldsymbol{r}_{\text{cm}} &= \sqrt{\frac{2 k_b T \mu^2}{2 \mu}}\, d\boldsymbol{W}_3(t), \\
&= \sqrt{2 \left(\frac{D}{2} \right)}\, d\boldsymbol{W}_3(t).
\end{aligned}
$$

This results in an effective diffusion coefficient, $D_{\text{cm}} = D/2$. Since the deterministic terms cancel, this is a purely stochastic differential equation. In other words, this is a continuous random walk

3

(Brownian motion). We can verify this by simulating the mean squared displacement of the center of mobility for all time. By definition, it should follow the relation

$$\langle \boldsymbol{r}_{\text{cm}}^2(t) \rangle = \left\langle \|\boldsymbol{r}_{\text{cm}}(t + t_0) - \boldsymbol{r}_{\text{cm}}(t_0)\|^2 \right\rangle = 2dD_{\text{cm}}t, \tag{5}$$

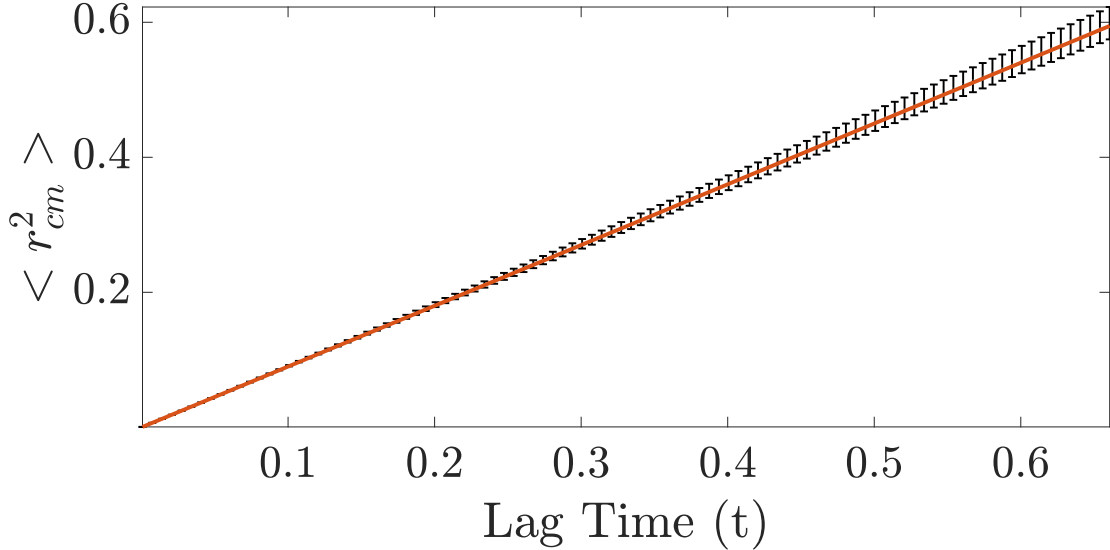where d is the dimension of $\boldsymbol{r}_{\text{cm}}$, and we are averaging across all t_0. In Fig. (1), a division of $2d$

Figure 1: Mean squared displacement of the centre of mobility averaged across t_0, given by (5). Error bars are shown in black and represent 95% confidence intervals. An approximate linear function $< r_{\text{cm}}^2 >= 2dD_{\text{cm}}t$ is plotted in orange. The simulated cross-linker has parameters $k = 10$, $a = 0.007$, $k_bT = 0.004$, $\eta = 0.1$, $l_0 = 0.5$, giving $D = 0.3$.

yields the expected diffusive coefficient $D_{\text{cm}} = 0.15$. This confirms that within statistical error, $\boldsymbol{r}_{\text{cm}}$ is entirely characterized by Brownian motion and we can therefore simulate the differential equation with low-order methods such as Euler-Maruyama. Statistical error was quantified by using the central limit theorem across multiple runs with different seeds to construct confidence intervals.

We must also transform our equations into an equation for $\boldsymbol{r}_{\text{d}}$, where $\boldsymbol{r}_{\text{d}} = \boldsymbol{r}_1 - \boldsymbol{r}_2$. Proceeding analytically, we can solve for $d\boldsymbol{r}_{\text{d}}$,

$$\begin{aligned}
d\boldsymbol{r}_{\text{d}} &= d\boldsymbol{r}_1 - d\boldsymbol{r}_2, \\
&= (\mu_1 \boldsymbol{F}_1 - \mu_2 \boldsymbol{F}_2)dt + \sqrt{2k_bT\mu_1}d\boldsymbol{W}_1 - \sqrt{2k_bT\mu_2}d\boldsymbol{W}_2, \\
&= \boldsymbol{F}_1(\mu_1 + \mu_2)dt + \sqrt{2k_bT(\mu_1 + \mu_2)}d\boldsymbol{W}_3, \\
&= \frac{k(l_0 - l)}{l}(\mu_1 + \mu_2)\boldsymbol{r}_{\text{d}}dt + \sqrt{2k_bT(\mu_1 + \mu_2)}d\boldsymbol{W}_3,
\end{aligned}$$

where l is the distance between $\boldsymbol{r}_1$ and $\boldsymbol{r}_2$, and l_0 is the rest length. We can see that there is an effective diffusion coefficient in this case as well, where $D_{\text{d}} = k_bT\mu_{\text{d}}$, and $\mu_{\text{d}} = \mu_1 + \mu_2$. Using this

4

notation, we can simplify to

$$dr_{\mathrm{d}} = \mu_{\mathrm{d}} \frac{k(l_0 - l)}{l} r_{\mathrm{d}} \, dt + \sqrt{2D_{\mathrm{d}}} \, dW_3. \tag{6}$$

The white noise in r_{d} obeys detailed balance, or microscopic time reversibility, and therefore the quantity r_{d} is ergodic with respect to the Gibbs-Boltzmann distribution, which is the solution of the Fokker-Planck or Kolmogorov forward DE at a steady state [3],

$$\frac{d}{dl}\left(\mu_{\mathrm{d}}\frac{k(l_0-l)}{l}r_{\mathrm{d}} \, P(l)\right) - k_b T \mu_{\mathrm{d}} \frac{d^2}{dl^2} P(l) = 0,$$

in one dimension. Analytically, it can be seen that the solution to this DE is the Gibbs-Boltzmann distribution

$$dP(l) = \frac{1}{Z} \exp\left(\frac{-k(l - l_0)^2}{2k_b T}\right) dl, \tag{7}$$

where Z is the normalizing factor. This can be extended to three dimensions, where $r_{\mathrm{d}} \in \mathbb{R}^3$. In spherical coordinates, with l, θ, ϕ corresponding to the radial distance, azimuthal angle, and polar angle respectively, we get

$$dP(l, \theta, \phi) = \frac{1}{Z} \exp\left(\frac{-k(l - l_0)^2}{2k_b T}\right) dV, \tag{8}$$

where, through the Jacobian, $dV = l^2 \sin\phi d\phi d\theta dl$. If we instead simulate the distribution of radial distances, a change in the probability measure gives us

$$dP(l) = \frac{1}{Z} l^2 \exp\left(\frac{-k(l - l_0)^2}{2k_b T}\right) dl. \tag{9}$$

Simulating the 1D scenario, as well as the 3D scenario measuring the radial distance, we get Fig.2 and Fig.3. We can see that both probability density functions are in agreement with the expected Gibbs-Boltzmann distribution.

2.2 Vibration and Rotation Model

In doing the above analysis, we have changed coordinate systems. We can change coordinate systems further, so that r_{d} is transformed into (u, l), where $l = \|r_{\mathrm{d}}\|$ represents the vibrational movement of the cross linker, and $u = r_{\mathrm{d}}/\|r_{\mathrm{d}}\|$ represents the dimers rotational movement. This can be done using the multidimensional Ito's Lemma [5]. This results in
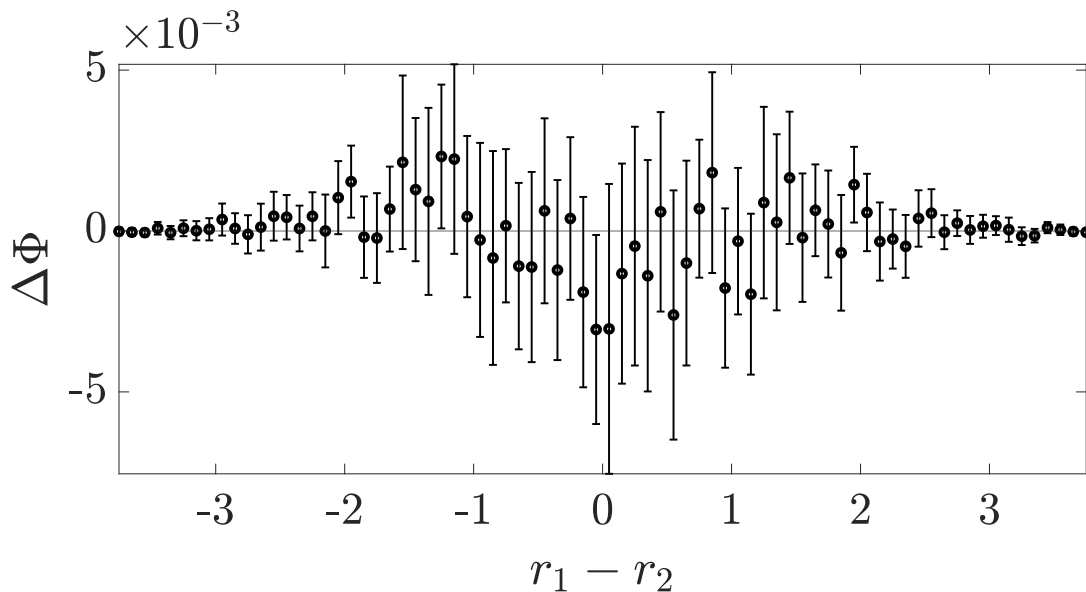
$$dl = \left(-(l - l_0)k\mu_{\mathrm{d}} + \frac{2k_b T \mu_{\mathrm{d}}}{l}\right) dt + \sqrt{2k_b T \mu_{\mathrm{d}}} \, dW_1, \tag{10}$$

$$du = \frac{-2k_b T \mu_{\mathrm{d}}}{l^2} u \, dt + \frac{\sqrt{2k_b T \mu_{\mathrm{d}}}}{l} u \times dW_2, \tag{11}$$

where dW_2 is a vector composed of d independent Wiener processes. Importantly, du rotates the cross linker on the unit sphere, i.e, $d\|u\| = 0$, and so $\|u\| = 1$ at all times.
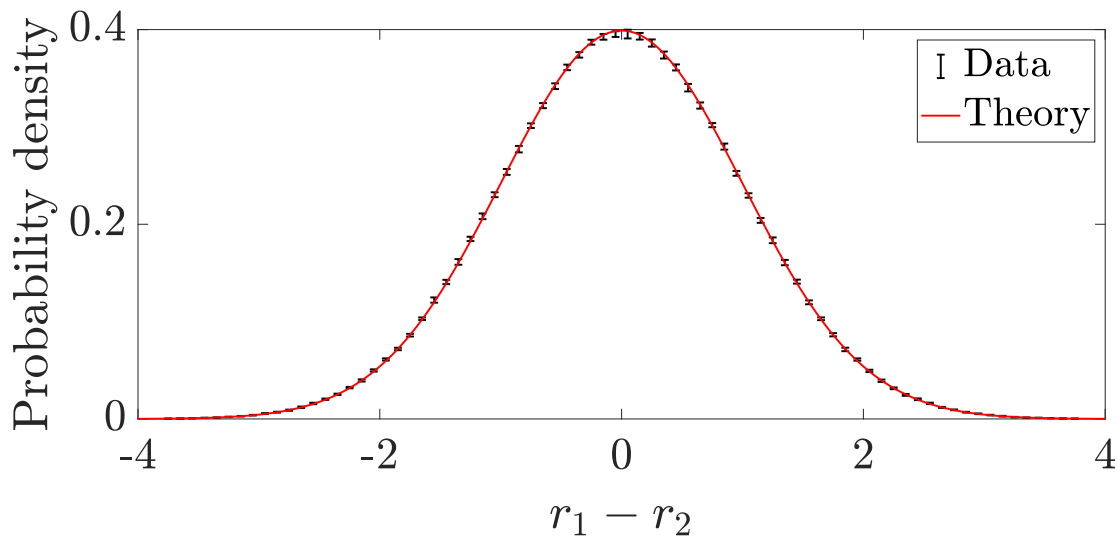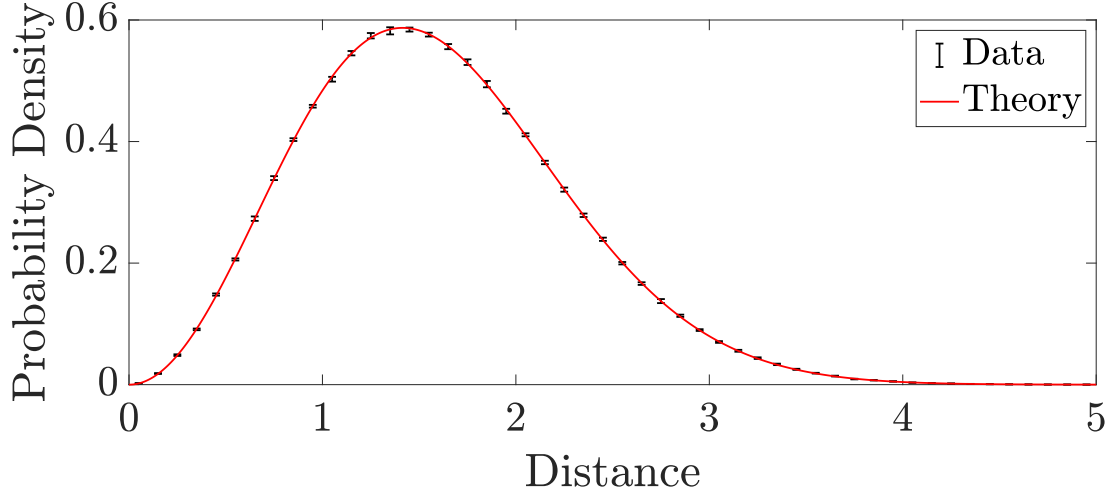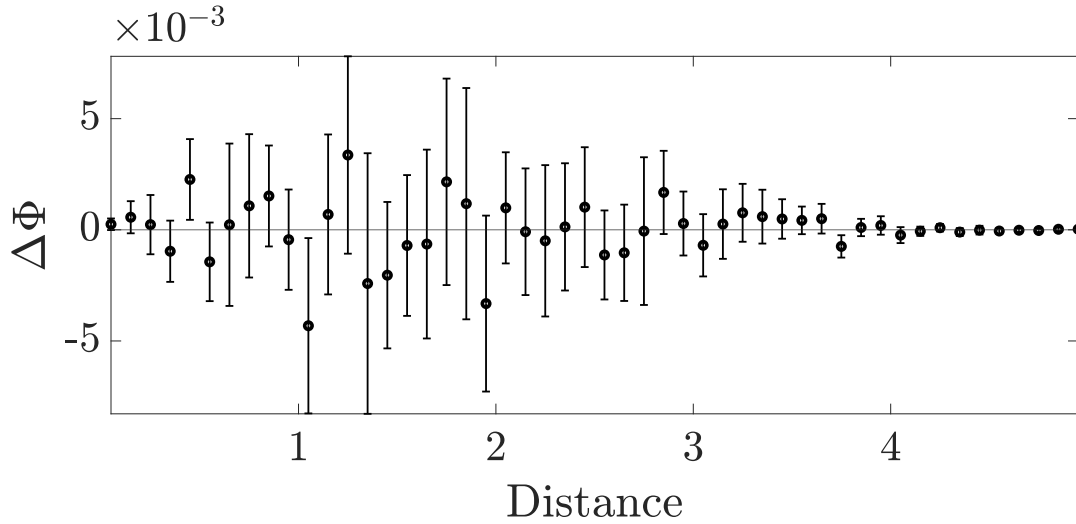
Figure 2: (a) Histogram of displacement between molecules r_1 and r_2 with rest length $l_0 = 0$, and parameters $k = 1$, $D = 1$, $\mu = 1$ in 1D, overlayed with the Gibbs-Boltzmann Distribution (7). (b) Comparison of numerical model with the Gibbs distribution. The vertical axis shows $\Delta\Phi$, the difference between the numerical model and the theoretical (Gibbs) distribution. Open circles represent the mean over 16 iterations. The 95% confidence intervals are shown by the error bars.

The biological plausibility of our model could be hindered by the approximation of cross linkers as dumbbells. A cross linker in our model is composed of two monomers connected by a spring, and the cross linker is free to diffuse in any direction. In reality, cross linkers are elongated molecules closer to cylinders, where movement parallel to the cross linkers' axis is more common than movement perpendicular to the cross linkers' axis. To model this, we introduce different

(a)

(b)

Figure 3: (a) Histogram of distance between molecules r_1 and r_2 with rest length $l_0 = 10^{-4}$, and parameters $k = 1$, $D = 1$, $\mu = 1$ in 3D, overlayed with the Gibbs-Boltzmann Distribution (9). (b) Comparison of numerical model with the theoretical distribution. The vertical axis shows $\Delta\Phi$, the difference between the numerical model and the theoretical Distribution. Open circles represent the mean over 16 iterations. The 95% confidence intervals are shown by the error bars.

mobilities for the vibrational diffusion ($\mu^{\parallel}$) and the rotational diffusion ($\mu^{\perp}$),

$$dl = \left(-2(l - l_0)k\mu^{\parallel} + \frac{4k_bT\mu^{\parallel}}{l}\right) dt + 2\sqrt{k_bT\mu^{\parallel}} \ dW_1, \tag{12}$$

$$d\boldsymbol{u} = \frac{-4k_bT\mu^{\perp}}{l^2}\boldsymbol{u} \ dt + \frac{2\sqrt{k_bT\mu^{\perp}}}{l}\boldsymbol{u} \times d\boldsymbol{W}_2. \tag{13}$$

It is important to note that these work out to be the same equations as (10) and (11) when $\mu_1 = \mu_2$, except here, $\mu^{\perp}$ takes the place of μ in (11), and $\mu^{\parallel}$ takes the place of μ in (10). This makes intuitive

sense, as movement in the parallel direction should not change $d\boldsymbol{u}$, and perpendicular movement should not change dl. When one end of the cross linker is bound, we reduce $\mu^{\parallel}$ and $\mu^{\perp}$ by a factor of two, to be consistent with the isotropic case, when $\mu^{\parallel} = \mu^{\perp}$. In the isotropic case, when one end of a cross linker binds actin, the mobility of that end would be set to 0.

3   NUMERICAL SIMULATION OF STOCHASTIC DIFFERENTIAL EQUATIONS

Now that we have created a model, we must find the best way to integrate our equations. To assess the convergence properties of our model, we will measure the convergence to the steady-state distribution from the evolution of $\boldsymbol{r}_{\mathrm{d}}$ that is expected from the Fokker-Planck equation.

By converting to $(\boldsymbol{r}_{\mathrm{d}}, \boldsymbol{r}_{\mathrm{cm}})$, we only need worry about the convergence properties of $\boldsymbol{r}_{\mathrm{d}}$, as we have previously shown that $\boldsymbol{r}_{\mathrm{cm}}$ has no deterministic term, and therefore is exact with the Euler-Maruyama scheme. However, we may wish to also simulate $\boldsymbol{r}_{\mathrm{d}}$ with Euler-Maruyama. Thus, given a stochastic differential equation of the form

$$d\boldsymbol{X}(t) = f(\boldsymbol{X}(t))dt + g(\boldsymbol{X}(t))d\boldsymbol{W}(t),$$

we can approximate the solution curve by discretizing the interval $[0, T]$ into $n = T/N$ intervals. Then $X_n = X(t_n)$, where t_n samples the left endpoint, consistent with Ito calculus. If an initial value is given, the Euler-Maruyama method approximates the solution by repeated iterations of

$$\boldsymbol{X}_{n+1} = \boldsymbol{X}_n + f(\boldsymbol{X}_n)\Delta t + g(\boldsymbol{X}_n)\Delta \boldsymbol{W}_n,$$

where $\Delta \boldsymbol{W}_n$ is a normally distributed random variable with mean 0 and variance Δt. Here we are only concerned with weak convergence. Thus, we will measure how the error of the expectation values decay as $\Delta t \to 0^+$. This means we need to define an error statistic. One choice (but not the only choice) would be to quantify the error statistic as

$$E = \left| \sqrt{\widehat{\mathrm{Var}(H)}} - \sigma \right|, \tag{14}$$

where, in 1D, σ is the standard deviation of the Gibbs distribution, or $\sqrt{k_b T / k}$, and $\widehat{\mathrm{Var}(H)}$ is the variance of the estimated histogram, H. If we set $k_b T = 1$, $k = 1$, then our new error statistic is simply the standard deviation of the numerically simulated histogram, minus 1. There is a weak order of convergence, γ if

$$E \leq C\Delta t^{\gamma},$$

for a constant C [4]. We could measure this error by plotting our error function against a dimensionless time step size, $\Delta \tau_s = \Delta t / \tau_s = \Delta t \mu_{\mathrm{d}} k$, where the time step size is a fraction of the relaxation time of the spring, $\tau_s = (\mu_{\mathrm{d}} k)^{-1}$, a fundamental time scale in our problem. Looking at Fig. 4, we see that the error of the second moment is approximately of order 1. It can also be seen that the statistical errors come to predominate over errors from the time step size.

We can contrast these results with those from using different numerical schemes. One scheme to look at is called the explicit midpoint scheme [2]. It is a predictor-corrector method. If we plan
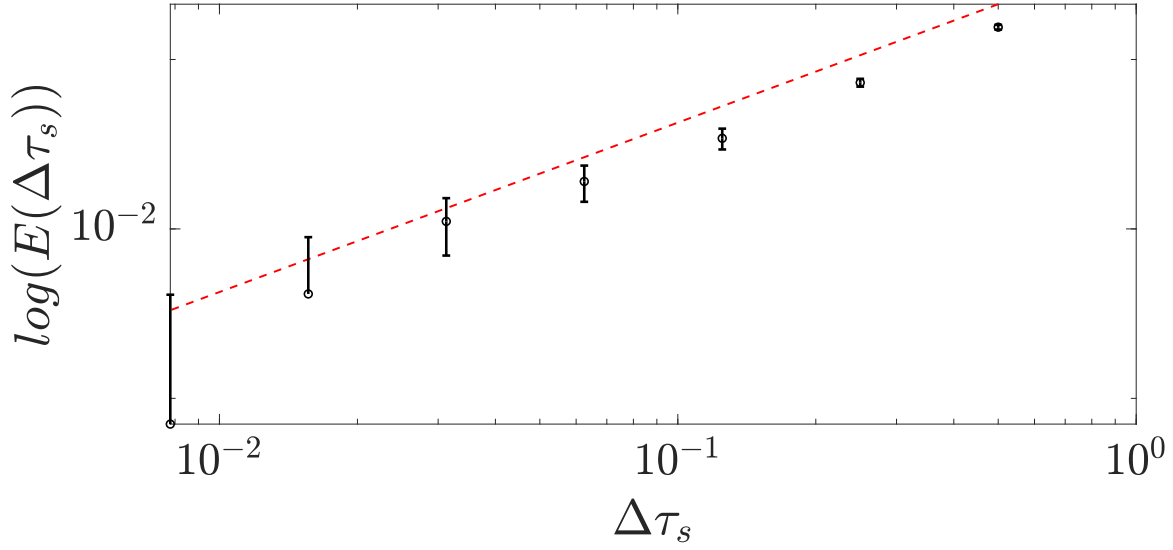
(a)
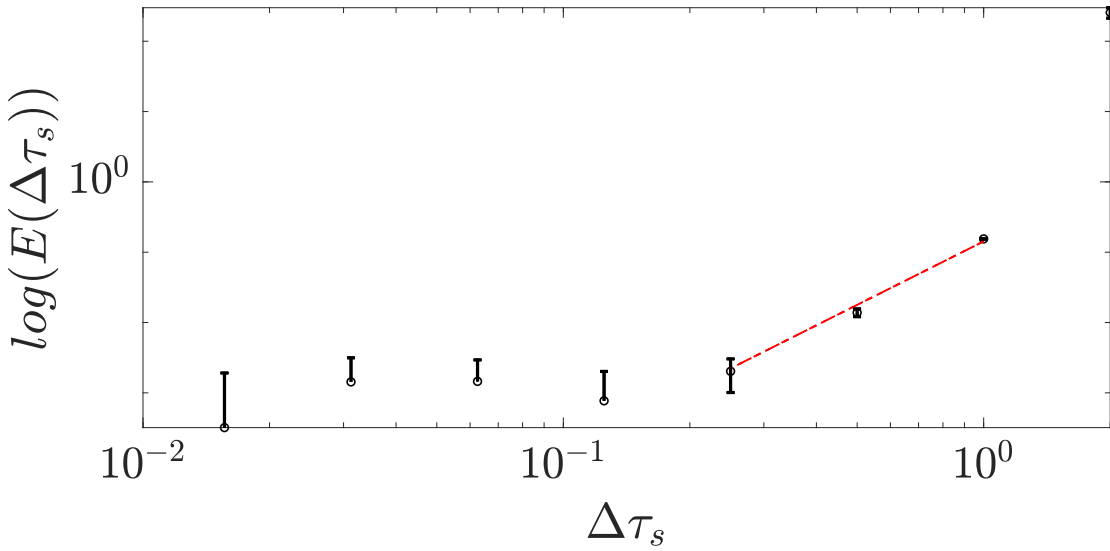
(b)

Figure 4: Error in spring length variance as defined by (14) as a function of the dimensionless time step, $\Delta\tau_s = \Delta t\mu_\mathrm{d}k$, where $\tau_s = \mu_\mathrm{d}k$, for (a) the Euler-Maruyama method in 1D, and (b) the explicit midpoint method in 1D. The power law reference functions are (a) $E \sim \Delta\tau_s$, (b) $E \sim \Delta\tau_s^3$ shown in red. Confidence Intervals are shown to 95% accuracy. Simulations were done with $k = 1$, $l_0 = 0$, $k_bT = 1$, $\mu_1 = \mu_2 = 1$, and ran over 100000 time steps for each of 16 trials. The relaxation time scale is $\tau_s = 1/(\mu_\mathrm{d}k) = 0.5$.

to simulate $\boldsymbol{r}_\mathrm{d}$, then given the function $L(\boldsymbol{r}_\mathrm{d}) = (\mu_1 + \mu_2)k(l_0 - l)/l$, where the dependence on $\boldsymbol{r}_\mathrm{d}$
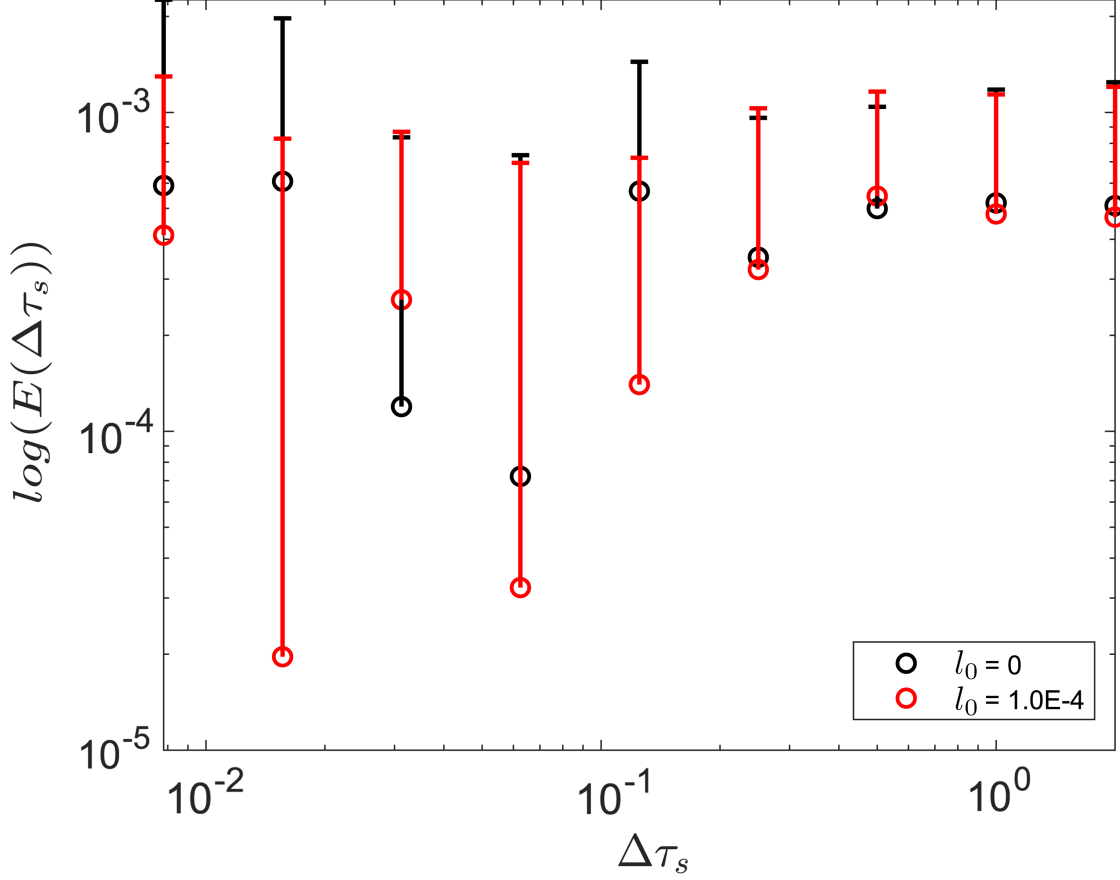
Figure 5: Error in spring length variance as defined by (14) as a function of the dimensionless time step, $\Delta\tau_s = \Delta t \mu_{\mathrm{d}} k$, where $\tau_s = \mu_{\mathrm{d}} k$, for the implicit trapezoidal scheme in 1D. Δt ranges from $\tau_s/2^7$ to $2\tau_s$. The results are shown for two different rest lengths. Confidence Intervals are shown to 95% accuracy. Simulations were done with $k = 1$, $k_b T = 1$, $\mu_1 = \mu_2 = 1$, and ran over 400000 time steps for each of 16 trials. The relaxation time scale, $\tau_s = 0.5$.

comes from $l = \|\boldsymbol{r}_{\mathrm{d}}\|$, we can define the following sequence

$$\boldsymbol{r}_{\mathrm{d}}^{p,n+\frac{1}{2}} = \boldsymbol{r}_{\mathrm{d}}^n + \frac{\Delta t}{2} L(\boldsymbol{r}_{\mathrm{d}}^n)\boldsymbol{r}_{\mathrm{d}}^n + \sqrt{D_{\mathrm{d}}\Delta t}\ \boldsymbol{W}_1,$$

$$\boldsymbol{r}_{\mathrm{d}}^{n+1} = \boldsymbol{r}_{\mathrm{d}}^n + \Delta t L(\boldsymbol{r}_{\mathrm{d}}^{n+\frac{1}{2}})\boldsymbol{r}_{\mathrm{d}}^{n+\frac{1}{2}} + \sqrt{D_{\mathrm{d}}\Delta t}\ (\boldsymbol{W}_1 + \boldsymbol{W}_2),$$

where $D_{\mathrm{d}} = k_b T(\mu_1 + \mu_2)$, $\boldsymbol{W}_i$ is a standard normally distributed vector, and the superscripts indicate either the point at which the quantity is evaluated, or whether it is a predictor step. We can see from Fig. 4b, that this demonstrates $O(\Delta t^3)$ convergence, but only until a certain point. Statistical errors come to predominate much faster than in the Euler-Maruyama scheme and the error drops much quicker as well. We can also use an implicit trapezoidal method [2] where we

follow the predictor-corrector scheme

$$r_{\mathrm{d}}^{p,n+1} = r_{\mathrm{d}}^n + \frac{\Delta t}{2} L(r_{\mathrm{d}}^n)(r_{\mathrm{d}}^n + r_{\mathrm{d}}^{p,n+1}) + \sqrt{2D_{\mathrm{d}}\Delta t}\, \boldsymbol{W}_1,$$

$$r_{\mathrm{d}}^{n+1} = r_{\mathrm{d}}^n + \frac{\Delta t}{2}\left(L(r_{\mathrm{d}}^n)r_{\mathrm{d}} + L(r_{\mathrm{d}}^{p,n+1})r_{\mathrm{d}}^{n+1} \right) + \sqrt{2D_{\mathrm{d}}\Delta t}\, \boldsymbol{W}_1.$$

Fig. 5. indicates that this may not necessarily follow a noticeable error relation as the other methods did. This method is in fact exact for the equilibrium distribution when $l_0 = 0$, as this results in $L(r_{\mathrm{d}}) = L \in \mathbb{R}$, i.e. there is no longer dependence on r_{d}. When $l_0 \neq 0$, the statistical errors continue to predominate, but this method is no longer exact.

4   STABILITY ANALYSIS

In numerical analysis, the other property we are concerned with is numerical stability. It is a theorem in stochastic calculus that the numerical stability of a stochastic differential equation is the same as the numerical stability of the corresponding deterministic differential equation. This can be seen by the following example. For a numerical method given by $\boldsymbol{X}_{n+1} = \boldsymbol{X}_n = M\boldsymbol{X}_n + \boldsymbol{K}\boldsymbol{N}$, where $\boldsymbol{K} \in \mathbb{R}^{d \times d'}$, $M \in \mathbb{R}$, and $\boldsymbol{N} \in \mathbb{R}^{d'}$ is a standard normally distributed vector. At a steady state we have

$$Var(\boldsymbol{X}_{n+1}) = \left\langle \boldsymbol{X}_{n+1}^2 \right\rangle - \left\langle \boldsymbol{X}_{n+1} \right\rangle^2,$$
$$Var(\boldsymbol{X}_{n+1}) = Var(\boldsymbol{X}_n),$$
$$\Rightarrow Var(\boldsymbol{X}_n) = \left\langle (M\boldsymbol{X}_n + \boldsymbol{K}\boldsymbol{N}) \cdot (M\boldsymbol{X}_n + \boldsymbol{K}\boldsymbol{N}) \right\rangle - \left\langle M\boldsymbol{X}_n + \boldsymbol{K}\boldsymbol{N} \right\rangle^2,$$
$$= \left\langle (M^2\boldsymbol{X}_n \cdot \boldsymbol{X_n} + M\boldsymbol{X}_n \cdot \boldsymbol{K}\boldsymbol{N} + (\boldsymbol{K}\boldsymbol{N}) \cdot (\boldsymbol{K}\boldsymbol{N}) \right\rangle - M^2 \left\langle \boldsymbol{X}_n \right\rangle^2,$$
$$= M^2 Var(\boldsymbol{X}_n) + \boldsymbol{K} \left\langle \boldsymbol{N}^T \boldsymbol{N} \right\rangle \boldsymbol{K}^T,$$
$$= \frac{\boldsymbol{K}\boldsymbol{K}^T}{1 - M^2},$$

which remains bounded for $|M| < 1$. This is the same stability criterion as for the corresponding deterministic equation. However, while M will tell us about stability, the accuracy criterion can be seen by also looking at the numerator, $\boldsymbol{K}\boldsymbol{K}^T$. So for the explicit midpoint method, with $l_0 = 0$, and in 1D, we are concerned with

$$\boldsymbol{X}_{n+1} = \boldsymbol{X}_n + \Delta t\left(-\mu_{\mathrm{d}}k\boldsymbol{X}_n + \frac{\Delta t}{2}\mu_{\mathrm{d}}^2 k^2 \boldsymbol{X}_n - \mu_{\mathrm{d}}k\sqrt{D_{\mathrm{d}}\Delta t}\boldsymbol{W}_1^n \right) + \sqrt{D_{\mathrm{d}}\Delta t}(\boldsymbol{W}_1^n + \boldsymbol{W}_2^n),$$
$$= \left(1 - \Delta t\mu_{\mathrm{d}}k + \frac{\Delta t^2 k^2 \mu_{\mathrm{d}}^2}{2} \right)\boldsymbol{X}_n + (1 - \Delta t\mu_{\mathrm{d}}k)\sqrt{D_{\mathrm{d}}\Delta t}\boldsymbol{W}_1^n + \sqrt{D_{\mathrm{d}}\Delta t}\boldsymbol{W}_2^n,$$
$$= \left(1 - \Delta\tau_s + \frac{\Delta\tau_s^2}{2} \right)\boldsymbol{X}_n + \sqrt{D_{\mathrm{d}}\Delta t((1 - \Delta\tau_s)^2 + 1)}\boldsymbol{W}_{12}^n,$$

so $M = (1 - \Delta\tau_s + \Delta\tau_s^2/2)$, and $|M| < 1 \iff 0 < \Delta\tau_s < 2$, which gives our stability region. This is consistent with Fig. 4, which shows instability at $\Delta t = 2\tau_s$. It is also seen that $K =$

$\sqrt{D_\mathrm{d}\Delta t((1 - \Delta\tau_s)^2 + 1)}$. Thus, $KK^T = D_\mathrm{d}\Delta t(1 - \mu_\mathrm{d}k\Delta t)^2 + D_\mathrm{d}\Delta t$, and we have

$$Var(\boldsymbol{X}_{n+1}) = \frac{D_\mathrm{d}\Delta t(1 - \mu_\mathrm{d}k\Delta t)^2 + D_\mathrm{d}\Delta t}{(1 - (1 - \Delta\tau_s + \Delta\tau_s^2/2)^2)},$$

$$\Rightarrow Var(\boldsymbol{X}_{n+1}) = Var(\boldsymbol{X}_n)\left(1 + \frac{1}{8}\Delta\tau_s^3 + O(\Delta\tau_s^4)\right),$$

where $Var(\boldsymbol{X}_n) = D_\mathrm{d}\tau_s = k_bT\mu_\mathrm{d}/(k\mu_\mathrm{d}) = k_bT/k$. This means that $Var(\boldsymbol{X}_{n+1})$ is correct to leading order $O(\Delta t^3)$. Therefore, a decrease in the time step size will decrease the variance by $O(\Delta t^3)$, which is consistent with our results from Fig. 4b.

5 QUANTIFYING THE EVOLUTION OF THE DIMER

In our model there are three time scales. There is the spring/relaxation time scale, which we have used above, τ_s, the rotational time scale, τ_r and the diffusive time scale, τ_d. The spring time scale is simply $1/(\mu_\mathrm{d}k)$, as the Ornstein-Uhlenbeck process for the spring length l has fluctuations about the rest length damped by

$$\langle(l(t + t_0) - l_0)(l(t_0) - l_0)\rangle = \frac{k_bT}{k}\exp\left(-\frac{|t|}{\tau_s}\right),$$

where $\tau_s = 1/(\mu_\mathrm{d}k)$.

However, we must also be able to keep track of rotational movement. In particular, once a cross linker has bound at one end to an actin polymer, the binding of the free end to another actin polymer will be driven by rotational diffusion. This quantity maintains the equilibrium statistical distribution of the overall orientation of the dimers, whereas translational diffusion maintains the equilibrium statistical distribution of the dimers' position in space. We can measure the rotational correlation time, τ_r, by looking at the decay of the auto-correlation function, given by

$$ACF(t) = \langle\boldsymbol{u}(t + t_0)\cdot\boldsymbol{u}(t_0)\rangle. \tag{15}$$

This function should decay at a rate inversely proportional to the rotational diffusion coefficient. For a rigid dimer made of equal particles it can be shown that

$$\langle\boldsymbol{u}(t + t_0)\cdot\boldsymbol{u}(t_0)\rangle = \exp\left(-2D_rt\right) = \exp\left(\frac{-2k_bTt}{3\pi\eta al_0^2}\right), \tag{16}$$

with the rotational diffusion coefficient, $D_r = k_bT\mu_\mathrm{r}$, where $\mu_\mathrm{r} = 2\mu/l_0^2 = \mu_\mathrm{d}/l_0^2$. Therefore, $ACF(t) = \exp(-2t/\tau_r)$, where $\tau_r = D_\mathrm{r}^{-1}$. We plot this relation in Fig. 6, and see that it is valid within statistical error. Note that with anisotropic mobilities, we get $\mu_\mathrm{r} = 2\mu^\perp/l_0^2$.

The third and final time scale is used in the SRBD algorithm itself, and it relates the reactive radius to the translational diffusion. Since each cross-linker cannot in a single time step diffuse farther than the distance of the actin-binding domain, we require $\Delta t \ll \tau_d = a_r^2/(k_bT\mu_\mathrm{cm})$, where a_r is the reactive radius of the actin-binding domain.

We have previously expressed our time step size, Δt, as a fraction of the spring time scale, but we can also extend this to the other two time scales in our problem, such that $\Delta\tau_r = \Delta t/\tau_r$ and $\Delta\tau_d = \Delta t/\tau_d$.

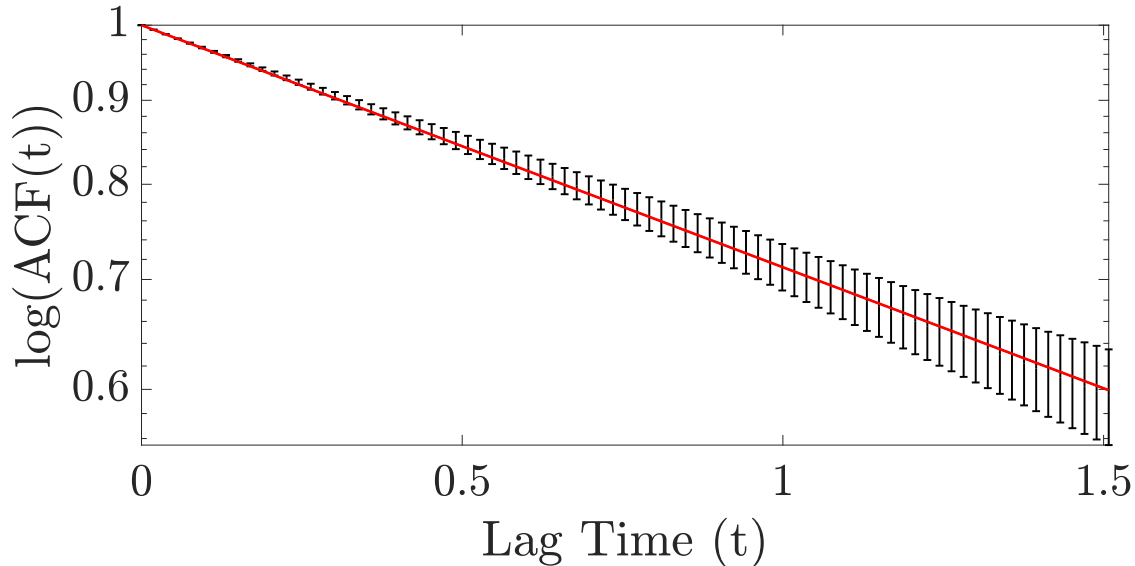Figure 6: Auto-correlation function $< \boldsymbol{u}(t + t_0) \cdot \boldsymbol{u}(t_0) >$, as a function of the lag time. The theoretical curve, $\exp(-2k_bTt/3\pi\eta al_0^2)$, is shown in red. Error bars are 95% confidence intervals. The simulation was ran with $k = 100$, $l_0 = 0.5$, $a = a_1 = a_2 = 0.01$, $\eta = 1.0$, and temperature chosen such that $k_bT = 4 \times 10^{-3}$.

In general, Δt must be smaller than the smallest time scale in order for convergence. Typically, and especially with a rigid dimer, the smallest time scale will be τ_s. However, in certain cases, the spring time scale may become negligibly small. This may occur when the spring is sufficiently stiff. Thus to satisfy $\Delta\tau_s \ll 1$, our time step size must also become unreasonably small. Therefore, as k becomes large, we are left with a stiff equation. This is not practical, so we simulate our model with $\Delta\tau_s > 1$ in a stiff limit, as explained below. We can derive the stiffness criterion by measuring the ratio

$$\frac{\tau_s}{\tau_r} = \frac{1/(k\mu_{\mathrm{d}})}{l_0^2/(2k_bT\mu_{\mathrm{d}})},$$

$$= \frac{2k_bT/k}{l_0^2},$$

$$\Rightarrow \tau_s = \left(\frac{\sqrt{2}\delta l}{l_0}\right)^2 \tau_r,$$

where δl is the fluctuation length of the spring. Therefore, as $\delta l^2 \ll l_0^2$, we enter the "stiff-spring" limit, where the spring time scale becomes negligible, and we are primarily focused on the rotational time scale (and also the diffusion time scale), as $\tau_s \ll 1$. In this limit the time scales τ_s and τ_r separate. It is clear that for these stiff systems, the explicit midpoint and Euler-Maruyama integrators will fail, as $\Delta\tau_s \propto \tau_s^{-1}$, which grows in proportion to k, and we have already shown a stability limit ($\Delta\tau_s < 2$) for the explicit midpoint method. One can show that the same relation holds for Euler-Maruyama, both numerically and analytically. However, it is less clear for the implicit trapezoidal method. Here, there is no stability limit, as is the case for most implicit solvers, but there may still be inaccuracies that arise when k becomes large enough. Fig. 7(c)

demonstrates that for a sufficiently stiff spring, and a large enough time step size, the implicit trapezoidal method fails to converge to the Gibbs distribution or to the correct rotational diffusion coefficient. Thus, the Euler-Maruyama, explicit midpoint, and implicit trapezoidal methods all fail to converge for large k and for a sufficiently large Δt. This is an issue, as dimers are often biologically modelled as stiff springs.

5.1 ROTATION AND VIBRATION INTEGRATOR

One way in which we could work around this issue is to separate the vibrational movement of r_d from the rotational movement of r_d. This has been accomplished by (10) and (11). In particular, rotation will be separate from vibration in the stiff limit. In addition, if a spring is stiff, l should be approximately constant. Thus, the relevant evolution of the dimer is rotational, not translational. By design, (11) measures only the rotation of the dimer, and the only relevant time scale is τ_r as τ_s is no longer a time scale involved in this equation. So we should not run into issues when τ_s separates from τ_r. We seek to find a way to simulate $d\boldsymbol{u}$ analytically, as if we can do so, we can efficiently capture the evolution of the dimer once it has bound actin. We use an Euler-Lie integrator which evolves Brownian motion on a spherical manifold and applies the action of SO(3).

We do this by rotating $\boldsymbol{u}$ by an angle $\theta = \sqrt{2D_\mathrm{d}\Delta t}\,\|\boldsymbol{N}\|\,/l$, where $\boldsymbol{N}$ is a normally distributed vector, and around an axis of rotation given by $\boldsymbol{k} = \boldsymbol{N}/\|\boldsymbol{N}\|$. The algorithm for rotating the vector $\boldsymbol{u}$ around this axis by an angle, θ, is given by the Rodrigues formula

$$\boldsymbol{u}_{n+1} = \boldsymbol{u}_n \cos\theta + (\boldsymbol{k} \times \boldsymbol{u}_n)\sin\theta + \boldsymbol{k}(\boldsymbol{k} \cdot \boldsymbol{u}_n)(1 - \cos\theta).$$

In Fig. 8(c), we can see that this method results in improved convergence to the steady state Gibbs distribution, as well as yields the correct rotational diffusion coefficient in the stiff limit.

However, when we are not in a stiff limit, the vibrational evolution of the dimer governed by (10) becomes increasingly relevant. We integrate this differential equation using the implicit trapezoidal method, except now we have an explicit term, $g(l) = 2D_\mathrm{d}/l + l_0\mu_\mathrm{d}k$, such that our predictor-corrector method becomes

$$l^{p,n+1} = l^n + \frac{\Delta t}{2}L(l^n)(l^n + l^{p,n+1}) + g(l^n)\Delta t + \sqrt{2D_\mathrm{d}\Delta t}\,\boldsymbol{W}_1, \tag{17}$$

$$l^{n+1} = l^n + \frac{\Delta t}{2}\left(L(l^n)l + L(l^{p,n+1})l^{n+1}\right) + g\left(\frac{1}{2}(l^n + l^{p,n+1})\right)\Delta t + \sqrt{2D_\mathrm{d}\Delta t}\,\boldsymbol{W}_1, \tag{18}$$

where $L(l) = -\mu_\mathrm{d}k$. However, the explicit term $g(\frac{1}{2}(l^n + l^{p,n+1}))$ can be evaluated differently. An alternative handling of the explicit term will lead to the corrector step

$$l^{n+1} = l^n + \frac{\Delta t}{2}\left(L(l^n)l + L(l^{p,n+1})l^{n+1}\right) + \frac{1}{2}(g(l^n) + g(l^{p,n+1}))\Delta t + \sqrt{2D_\mathrm{d}\Delta t}\,\boldsymbol{W}_1. \tag{19}$$

While this alternative handling of the explicit term will converge to the Gibbs-Boltzmann distribution for small Δt, this is not generally true as Δt grows. Indeed the former approach is more accurate, as it is minimizes error for small l, as shown in Fig. 9(b).
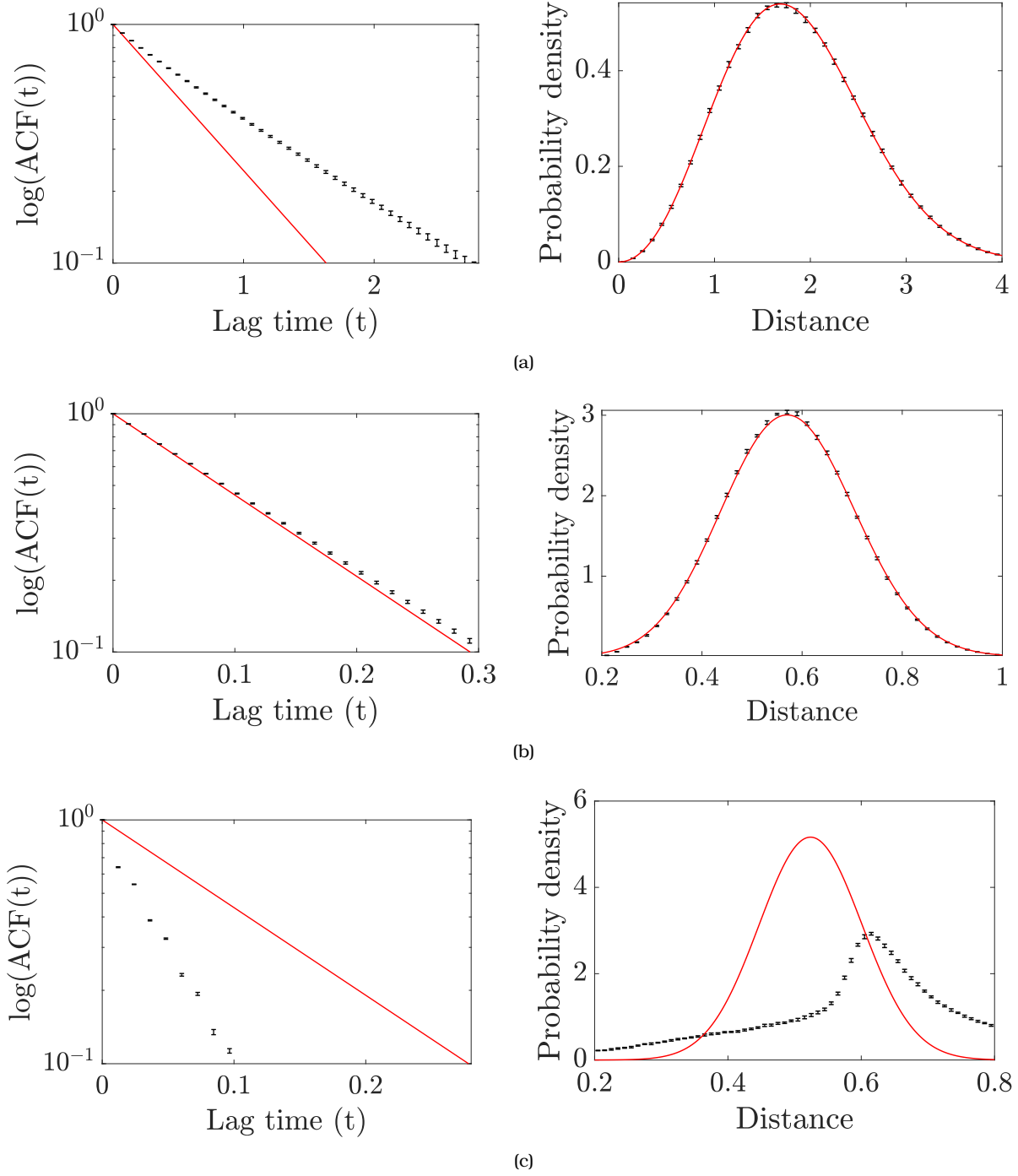
(a)

(b)

(c)

Figure 7: Auto-correlation function $< \boldsymbol{u}(t + t_0) \cdot \boldsymbol{u}(t_0) >$, as a function of the lag time, t, plotted beside the histogram for the evolution of $\boldsymbol{r}_{\mathrm{d}}$ with various spring constants. (a) $k = 0.1$, $\Delta\tau_s = 0.0125$, $\delta l/l_0 = 2$, (b) $k = 5$, $\Delta\tau_s = 0.625$, $\delta l/l_0 = 0.282$ (c) $k = 16$, $\Delta\tau_s = 2$, $\delta l/l_0 = 0.158$. Theoretical curve is given by (16) for (a), (b), (c), and shown in red. Simulations ran with the implicit trapezoidal method and $\Delta\tau_r = 0.1$, $a_1 = a_2 = 0.01$, $\eta = 1.0$, $l_0 = 0.5$, $k_b T = 0.1$. The time scale τ_r was computed in the stiff limit, and $\Delta\tau_s = 0.1\tau_r/\tau_s$.

(a)

(b)

(c)
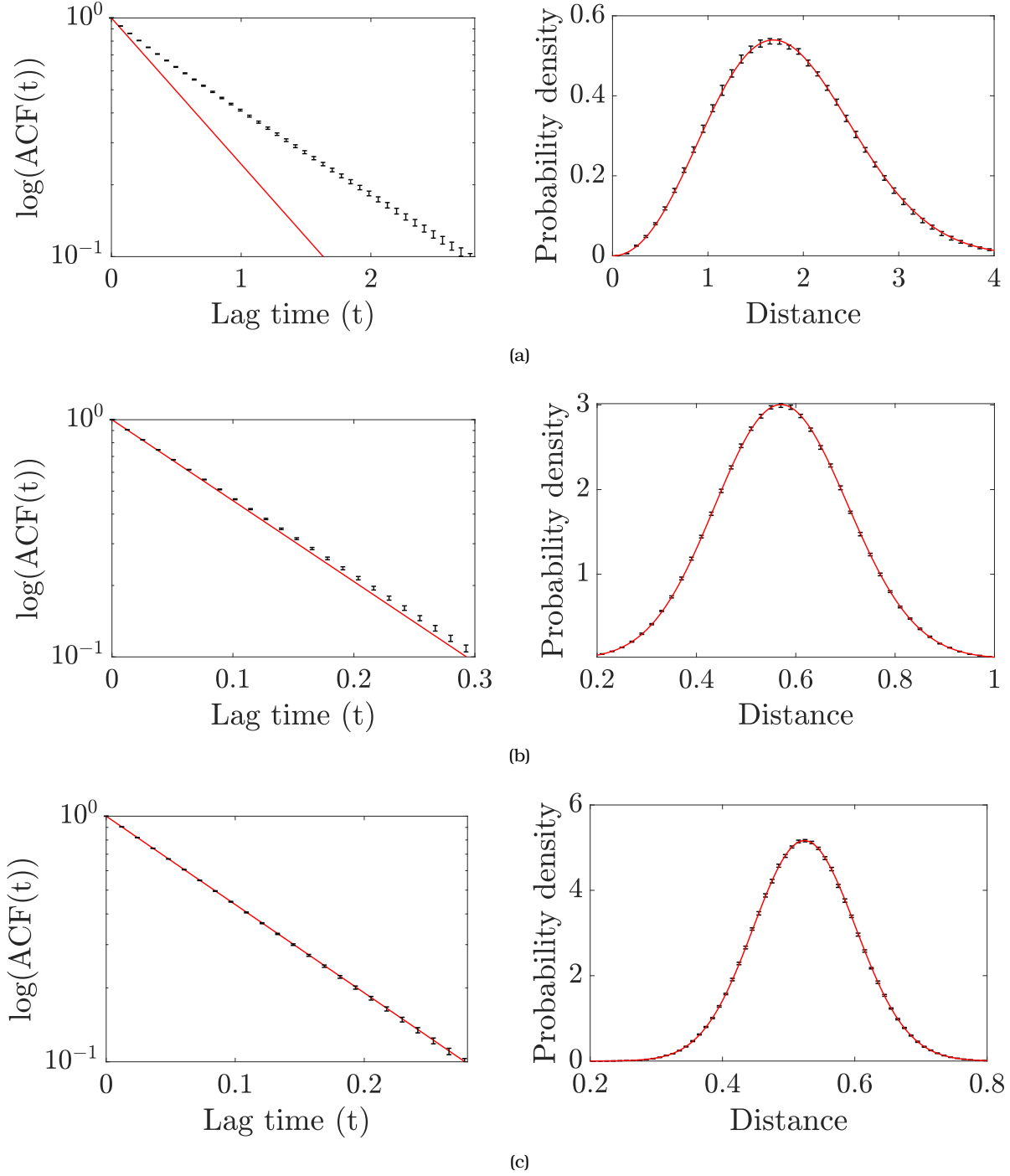
Figure 8: Auto-correlation function $< \boldsymbol{u}(t + t_0) \cdot \boldsymbol{u}(t_0) >$, as a function of the lag time, t, plotted besides the histogram for the evolution of $\boldsymbol{r}_\mathrm{d}$ with various spring constants. (a) $k = 0.1$, $\Delta\tau_s = 0.0125$, $\delta l/l_0 = 2$, (b) $k = 5$, $\Delta\tau_s = 0.625$, $\delta l/l_0 = 0.283$ (c) $k = 16$, $\Delta\tau_s = 2$, $\delta l/l_0 = 0.158$. Theoretical curve is given by (16) for (a), (b), and (c), and is shown in red. Simulations ran with the separation of vibration and rotational time scales method and $\Delta\tau_r = 0.1$, $a_1 = a_2 = 0.01$, $\eta = 1.0$, $l_0 = 0.5$, $k_b T = 0.1$. The time scale τ_r was computed in the stiff limit, and $\Delta\tau_s = 0.1\tau_r/\tau_s$.
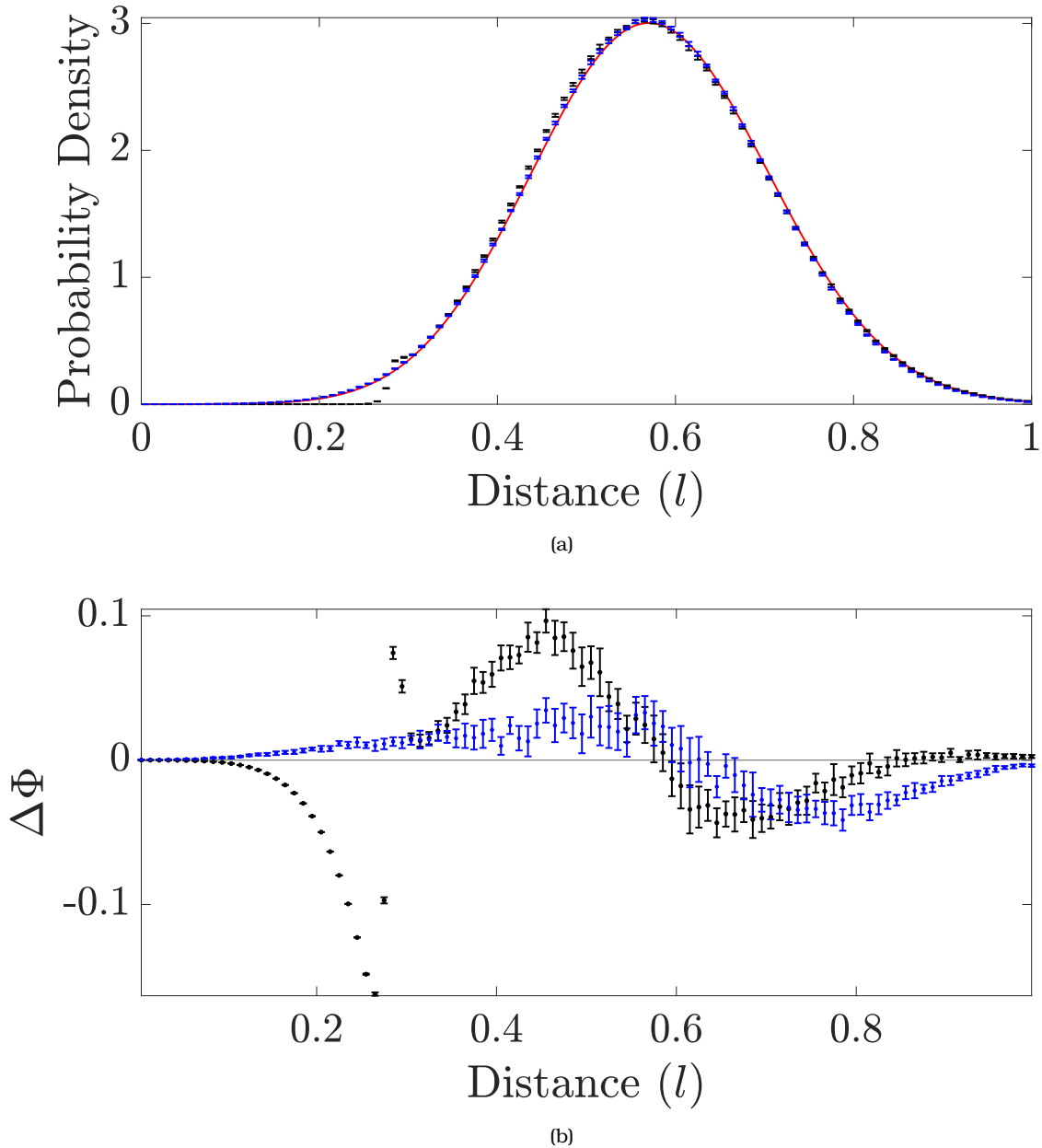
16

Figure 9: (a) Convergence to the Gibbs-Boltzmann distribution, shown in red. (b) Comparison of numerical model and the theoretical distribution. The vertical axis shows $\Delta\Phi$, the difference between the numerical model and the theoretical distribution. Parameters were $k = 5$, $k_bT = 0.1$, $a_1 = 0.01$, $a_2 = 0.01$, $\eta = 1.0$, $l_0 = 0.5$, $\delta l/l_0 \approx 0.28$, $\Delta\tau_r = 0.25$, $\Delta\tau_s = 3.375$. Simulations were ran with the separation of vibration and rotation time scales method using the corrector scheme (19) in black, and the corrector scheme (18) shown in blue. Error bars represent 95 % confidence intervals.

5.2 ROTATION AND VIBRATION IN AN ANISOTROPIC SETTING

Using (12) and (13), we can extend our model to include anisotropic mobilities. In our code, we are using the convention $\mu_1 = 2\mu_{cm} = 2\mu^\perp/3 + \mu^\parallel/3$, and $\mu_2 = \mu^\perp$. Thus, $\mu^\parallel = 3\mu_1 - 2\mu_2$. Note that

if $\mu^{\|} \neq \mu^{\perp}$ then this is a separate convention from the isotropic case, where μ_1 and μ_2 referred to the mobilities of $\boldsymbol{r}_1$ and $\boldsymbol{r}_2$, respectively. If $\mu^{\|} = \mu^{\perp}$, then these conventions are consistent with each other. However, using the anisotropic convention, we get the results shown in Fig. 10, which demonstrates that we are able to successfully generalize to a setting with anistropic mobility.
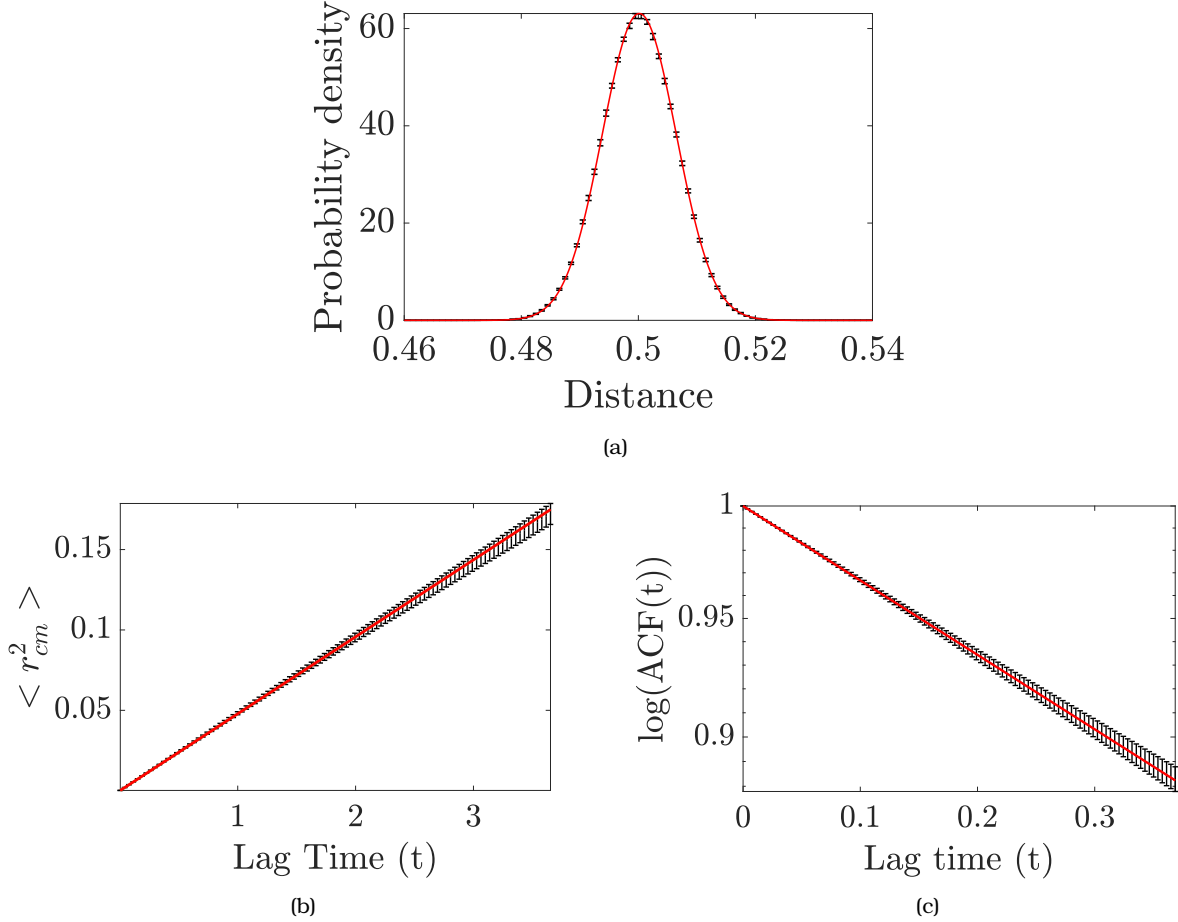

(a)

(b)

(c)

Figure 10: Comparison of data (black) to theoretical results (red) for (a) the Gibbs-Boltzmann distribution (9), (b) the diffusion of the center of mobility (5), and (c) the auto-correlation function, as a function of the lag time, (t), (16). Parameters were $\mu^{\perp} \approx 5.31$, $\mu^{\|} \approx 1.40$, $k = 100$, $k_b T = 4.0 \times 10^{-3}$, $a_1 = 0.0133$, $a_2 = 0.01$, $\eta = 1.0$, $\delta l/l_0 \approx 0.006$. Simulations were ran with the separation of vibration and rotation time scales method. Error bars represent 95 % confidence intervals.

5.3 ROTATIONAL DIFFUSION IN THE NON-STIFF LIMIT

The relation given by (16) is only valid in a stiff limit. In the non-stiff limit, we expect there to be a correction ratio r, such that for a dimer of equal radii

$$\langle \boldsymbol{u}(t + t_0) \cdot \boldsymbol{u}(t_0) \rangle = \exp\left(\frac{-2k_b T t r}{3\pi \eta a l_0^2}\right). \tag{20}$$

This ratio is given by

$$r = \left\langle \frac{l_0^2}{l^2} \right\rangle = l_0^2 \frac{\int_0^\infty \exp\left(-(l-l_0)^2/(2\delta l^2)\right) \, dl}{\int_0^\infty l^2 \exp\left(-(l-l_0)^2/(2\delta l^2)\right) \, dl},$$

$$\Rightarrow r = \frac{\sqrt{2\pi}(\mathrm{erf}(\sqrt{2}/(2x)) + 1)}{\sqrt{2\pi}(x^2 + 1)\,\mathrm{erf}\left(\sqrt{2}/(2x)\right) + 2\exp(-1/(2x^2))x + \sqrt{2\pi}(x^2 + 1))}, \tag{21}$$

where $x = \delta l/l_0$. However, when we plot this relation in Fig. 11, we can see that the slope does not perfectly match the data. In fact, for $\delta l \gg l_0$, the decay is not exponential. We postulate that
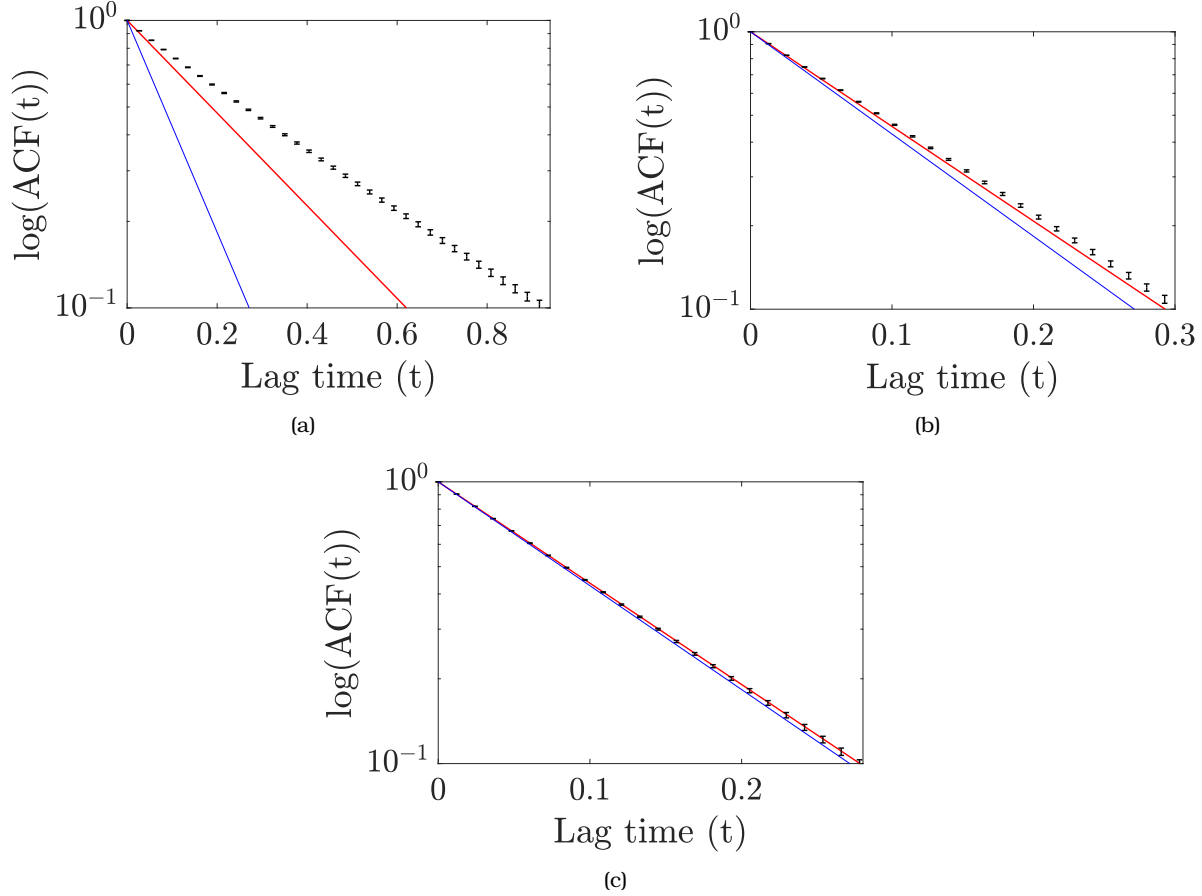

(a)

(b)

(c)

Figure 11: Auto-correlation function $< \boldsymbol{u}(t + t_0) \cdot \boldsymbol{u}(t_0) >$, as a function of the lag time, (t). **(a)** $k = 0.4$, $\delta l/l_0 = 1$, **(b)** $k = 5$, $\delta l/l_0 = 0.282$ **(c)** $k = 16$, $\delta l/l_0 = 0.158$. Theoretical curve for a stiff spring (18) is shown in blue, while the theoretical curve for a non-stiff spring (21) is shown in red. Simulations ran with the separation of vibration and rotational time scales method and $\Delta\tau_r = 0.1$, $a_1 = a_2 = 0.01$, $\eta = 1.0$, $l_0 = 0.5$, $k_bT = 0.1$. Error bars represent 95 % confidence intervals.

there may in fact be two exponentials, one for short time, and one for long time, and some sum of these exponentials is the true theoretical curve. In the stiff limit, this sum may converge to a single exponential, that as seen in (16). This is still an area of active research.

6 Conclusions

We have expanded upon the Stochastic Reactive Brownian Dynamics (SRBD) algorithm to include the simulation of dimers. In doing so, we developed a new set of integrators which minimize numerical instabilities and allow us to analytically solve key steps in the relevant evolution of the dimer. Our model is reaction-limited, so we diffuse the center of mass analytically to capture translational diffusion, minimizing the cost of this step in our algorithm. In addition, our Euler-Lie integrator evolves Brownian motion on the unit sphere and analytically solves for the rotational movement of the dimer, which has increasing importance once a dimer had bound actin. By developing a model which has reduced numerical inaccuracies, we can efficiently simulate actin cross linking. This is important as it is aligned with a fundamental goal of statistical mechanics: to build models of microscopic phenomena to explain mesoscopic behavior. Our long term goal is to use this model to explain this mesoscopic behavior that has been experimentally measured in the cell.

Next steps include adding reverse reactions to visualize and measure unbinding of the cross linkers, and measuring the rate at which cross linkers bind actin in different geometries. In addition, we wish to make quantitative computations with our dimers represented as cylinders rather than dumbbells. In particular, an open question is whether the macroscopic rate of binding will decrease significantly when anisotropic mobilities are included.

REFERENCES

1. Et. al, A. D. Efficient Reactive Brownian Dynamics. *The Journal of Chemical Physics,* 034103 (2018).

2. Et. al, S. D. Multiscale Temporal Integrators for Fluctuating Hydrodynamics. *Physical Review. E, Statistical, Nonlinear, and Soft Matter Physics,* 063312 (2014).

3. Graham, M. D. *Microhydrodynamics, Brownian Motion, and complex fluids* (Cambridge University Press, 2018).

4. Higham, D. J. An Algorithmic Introduction to Numerical Simulation of Stochastic Differential Equations. *SIAM Review,* 525–546 (2001).

5. Higham, D. J. & Kloeden, P. E. *An Introduction to the Numerical Simulation of Stochastic Differential Equations* (Society for Indsutrial and Applied Mathematics, 2021).